2017-01-01

Bottom trapped internal waves over the Malin Sea continental slope

Stashchuk, Nataliya

http://hdl.handle.net/10026.1/8640

10.1016/j.dsr.2016.11.007
Deep Sea Research Part I: Oceanographic Research Papers
Elsevier BV

Bottom trapped internal waves over the Malin Sea continental slope

Nataliya Stashchuk[a], Vasiliy Vlasenko[a],

[a]*School of Marine Science and Engineering, University of Plymouth, Drake Circus, Plymouth, PL4 8AA, UK*

Abstract

Three-dimensional dynamics of internal tides on the continental slope of the Malin Sea is studied numerically and validated with the observational data collected on the 88-th cruise of the RRS "James Cook" in June-July 2013. Observed in-situ bottom intensification of baroclinic tidal currents was reproduced in a series of numerical experiments using the Massachusetts Institute of Technology general circulation model. The baroclinic tidal dynamics is explained in terms of superposition of two wave processes developing in the area. One of them is a tidal beam generated at the shelf break and radiating tidal energy downward into abyss. The second important process identified here was a bottom trapped internal wave, generated by the tidal flow over a local prominence. This internal wave was trapped by the topography at the depths below 800 m and propagated northward along the slope.

Key words: Baroclinic tides, bottom trapped internal waves, the Malin Sea

1. Introduction

The Malin Sea is a marginal sea boundering the lowlands of Scotland and Ireland. It covers the area restricted by 57°N latitude at the north and 10°W longitude at the west. The main part of the Malin Sea is shallow with the depths typically ranging between 150 and 200 m. Offshore the continental slope is steep at the south (supercritical to internal M_2 tide) and has a number of small-scale canyons and a large-scale indentations between 55.5 and 55.8°N, Figure 1.

The spatial variability of the bottom topography along the slope suggests existence of a variety of three-dimensional dynamical processes developing in the area that can take the form of barotopic and baroclinic tides, short-scale internal waves, quasi-stationary currents and mesoscale eddies. Historically, most of previous in-situ observations were focussed on the analysis of cross shelf/slope variability of internal tides and tidally generated internal waves (*Sherwin* (1988); *Small et al.* (1999a); *Hallock et al.* (2000); *Small* (2003)) and their effect on the marine environment (*Inall et al.*, 2000, 2001; *Rippeth and Inall*, 2002). Even though a three-dimensional nature of generated wave was obvious in the results of the SESAME experiment (*Small et al.*, 1999a), specifically, in SAR images of recorded internal wave packets, the interpretation of the observational data was conducted based basically either on a two-dimensional theory (*Stashchuk and Vlasenko* (2005)), or in terms of the mechanism of refraction of internal waves (*Small* (2000, 2003)). The three-dimensional structure of observed internal waves was not the focus of these studies. It is worth mentioning that the experimental studies in the area mostly ignored an along slope variability, although the paper by *Souza* *et al.* (2001) investigated a water transport along the Malin shelf/slope, and the JEBAR effect was acknowledged there as a dominant mechanism causing slope currents.

One of the first efforts on modelling of baroclinic tides in the Malin shelf/slope area was undertaken by *Sherwin and Taylor* (1990) who used their two-dimensional slice model to reproduce the baroclinic tidal characteristics in the area. The model showed amplification of the baroclinic tidal signal near the bottom over the continental slope (presumably due to a baroclinic tidal beam), but their comparison with observations have been classified as inconclusive. Another attempt to build a sigma-coordinate numerical model suitable for investigation of internal tides generation in three dimensions was reported by *Xing and Davies* (1997). Their model was applied to the Malin shelf-slope area, but since the runs were restricted to a two-dimensional topography the meridional variability of internal tides could not be investigated. Note, however, that the most remarkable feature of the baroclinic tide there, viz. generation of an internal tidal beam over supercritical topography, was clearly demonstrated in (*Xing and Davies*, 1997, 1998). Some more details on the role of internal tide in enhancement of internal mixing and formation of the thermohaline structure of waters on the Malin Shelf were reported by *Xing et al.* (1999), but again, the three-dimensional effects of internal tides remained beyond the scope of this study.

Lack of understanding of the along slope variability of the dynamical processes developing in the area was a strong motivation for the 88-th cruise of RRS "James Cook" (hereafter JC88) to the Malin shelf-slope area conducted in June-July 2013 in the framework of the NERC funded project

FASTNEt (UK). It was also assumed that the observational data set will be complemented by the results of three-dimensional modelling using the Massachusetts Institute of Technology general circulation model (hereafter MITgcm). This paper reports the results of the modelling efforts on replication of the processes developing in the area including baroclinic tides and bottom trapped internal waves. The model output is validated against the observational data collected during the JC88 cruise. The rest of the paper is organized as follows. A short description of the field campaign is presented in Section 2. Section 3 briefly outlines the model details. Section 4 discusses the generation mechanism of internal tides relevant to the present study. Section 5 presents the principal part of the modelling results with their comparison against collected observational data. Section 6 summarises all basic findings on bottom trapped internal waves. Some necessary theory to underpin formulated conclusion on theoretical and observational evidence of bottom trapped internal waves is presented in Section 7. The paper ends up with Summary and Conclusion presented in Section 8.

2. Observations

The principal objective of the JC88 cruise to the Malin Sea (28 June - 24 July, 2013) was investigation of cross-shelf transport and vertical mixing induced by internal tide and mesoscale dynamical processes developing in the area. In doing so 73 CTD stations were conducted on the shelf and over the continental slope. Each CTD cast was accompanied by velocity measurements using a 300 kHz Lowered Acoustic Current Profiler (LADCP) mounted on the CTD probe frame. The CTD survey was conducted along three cross-sections shown in Figure 1. The positions of sampling stations are shown by green dots. Measurements along the middle and northern sections (sections 2 and 3, respectively) were conducted twice, with some stations repeated at the very same positions. Observational data from the stations depicted in Figure 1 by numbers are used for the present analysis; their details are presented in Table 1.

In addition to the stations, 14 moorings equipped with ADCPs were deployed in the area. The velocity time series recorded at four of them located over the continental slope, La, Lb, Sb, and Sd, are used in this study for the model validation. Two types of current meters were mounted at the moorings: 300 kHz ADCPs provided samplings at a rate 15 sec over a period of several weeks; sampling intervals of 75 kHz ADCPs varied from 2.5 to 60 min (depending on the device position). More details on the sampling intervals and moorings position are presented in Table 2.

3. Model set-up

The collected in-situ data were complemented by the results of numerical modelling conducted using the MITgcm. The central part of the model domain is shown in Figure 1 by a blue rectangle. It includes a 536×536 model grid with horizontal resolution 150 m in zonal and meridional directions. In addition to the central part, 200 grid steps were added to each boundary of the model grid transforming it into a 936×936 grid. In these extra lateral areas the grid resolution varied gradually from 150 m in its central part to 50 km near the boundaries. Such a telescopic increase of the horizontal steps towards the periphery makes physical size of the domain big enough to exclude any reflections of the waves from the model boundaries for at least 10 tidal cycles. The vertical grid step was equal to 10 m.

The model was forced by barotropic tidal terms added to the right hand side of the momentum balance equations. The parameters of eight principal tidal harmonics

$$
\begin{aligned}
U_j &= A_j \cos(\omega_j t - \vartheta_j), \\
V_j &= B_j \cos(\omega_j t - \theta_j),
\end{aligned}
$$

$(j = 1, 2, \cdots, 8)$ are shown in Table 3. Zonal and meridional tidal discharges U_j and V_J with amplitudes A_j and B_j as well as tidal phases ϑ_j and θ_j for each tidal harmonic ω_j were taken from the output of the inverse tidal model TPXO8.1 (*Egbert and Erofeeva*, 2002).

It worth mentioning that the principal target of the present study is tidally induced deep-water dynamics. All processes developing in the upper layer generated by ocean-atmosphere interaction (wind-driven circulation, inertial oscillations), or slope currents initiated by horizontal pressure gradients, as well as many other non-stationary processes of different nature were not an objective of the present study. Such an approach can be justified by an overwhelming predominance of tidal motion in the area, although some discrepancy between in-situ recorded and model predicted signals is expected.

After the MITgcm was configured, it was run in its barotropic mode (without vertical stratification of the fluid) to reproduce tidal currents; the latter were compared against the TPXO8.1 output for consistency. The forcing parameters were adjusted in such a way to achieve the best fit of both models.

After validation with the TPXO8.1, the MITgcm was run with realistic fluid stratification. The data on the background temperature and salinity distributions were taken from the CTD survey conducted during JC88 cruise. A resulting vertical profile of the background buoyancy frequency averaged over the whole set of the CTD stations is shown in the inset in Figure 1.

The vertical turbulent closure for the coefficients of vertical viscosity ν and diffusivity κ was provided by the Richardson number dependent parameterization (*Pacanowski and Philander*, 1981):

$$\nu = \frac{\nu_0}{(1+\alpha \mathrm{Ri})^n} + \nu_b, \quad \kappa = \frac{\nu}{(1+\alpha \mathrm{Ri})} + \kappa_b.$$

Here $\mathrm{Ri} = N^2(z)/(u_z^2 + v_z^2)$ is the Richardson number, and $N^2(z) = -g/\rho(\partial\rho/\partial z)$ is the buoyancy frequency (g is the acceleration due to gravity, and ρ is the density), u and v are zonal and meridional components of horizontal velocities, respectively; ν_b=10^{-5} m^2 s^{-1} and κ_b=10^{-5} m^2 s^{-1} are the background parameters, ν_0=$1.5 \cdot 10^{-2}$ m^2 s^{-1}, α=5 and n=1 are the adjustable parameters. Such a parameterization increases coefficients ν and κ in the areas where the Richardson number is small which should take into account the mixing processes induced by the shear instabilities and breaking internal waves. The horizontal viscosity A^h and diffusivity K^h were taken at the level of $0.5\,\mathrm{m}^2\,\mathrm{s}^{-1}$.

An extra block was added to the MITgcm that recorded velocities (from surface to the bottom) with 1 min sampling interval at four grid points that coincided with the positions of La, Lb, Sb, and Sd moorings (see Figure 1).

4. Qualitative analysis of the generation mechanism

The regime of generation of internal waves by tide interacting with bottom topography depends on its relative steepness. In a two dimensional case the ratio of the maximum of the bottom steepness $\gamma = dH/dx$ ($H(x)$ is the water depth) to the inclination α of the characteristic lines of the wave equation,

$$\alpha(z) = dz/dx = \pm[(\omega^2 - f^2)/(N^2(z) - \omega^2)]^{1/2},$$

(here f is the Coriolis parameter) is a measure of the modal content of the generated wave fields. The bottom is considered as a gently sloping one when the inclination of characteristic lines α substantially exceeds the bottom inclination γ. In such a case the lowest baroclinic modes are generated with the first mode being predominant.

In the areas with steep topographies where $\gamma = \alpha$ (critical case) or $\gamma > \alpha$ (supercritical conditions) a large number of baroclinic modes with comparable amplitudes are generated. The superposition of the generated modes leads to the formation of a tidal beam, i.e. a relatively narrow wave guides along which the baroclinic tidal energy radiates from the bottom (*Vlasenko et al.*, 2005). The baroclinic wave energy in tidal beams is concentrated along the characteristic lines $x = \pm \int dz/\alpha(z) + \text{const}$.

In our case considerable part of the Malin Slope below 500 m isobath is supercritical for the semi-diurnal tide. This is clearly seen in Figure 2 where the characteristic lines are shown as pink stripes of different thickness for three chosen sections depicted in Figure 1. The thickness of these lines represents an intensity of tidal beams. In fact, the amount of tidal energy converted from barotropic to baroclinic modes and concentrated inside the beam depends on the size of the area of the bottom topography that satisfy near-critical conditions, i.e. $\gamma \sim \alpha$.

Sharp edges in this respect (e.g. step-wise topography) produce sharper but much weaker tidal beams than smoothly convex bumpy topographies. In application to the considered area, sections 1 and 2 shown in Figure 2 with near-critical conditions in wide sectors (**a**)-(**b**) and (**c**)-(**d**), respectively, can produce much stronger tidal beam than narrow edge-type area (**e**)-(**f**) shown in section 3.

This reasoning can be helpful in interpretation of observational data and model results. Having known the positions of moorings and CTD stations with respect to the tidal beam as show in Figure 2, one can expect a higher level of tidal signal at depths where CTD station or mooring crosses the beam.

5. Comparison of observational and model data

Comparative analysis of in-situ and model data is conducted separately for sections 1, 2, and 3 shown in Figure 1.

Section 1.

Figure 3 represents model predicted zonal u and meridional v velocities (left and central panels, respectively) calculated for the time t=85 h of the model run. As it is expected from the preliminary qualitative analysis, both velocity sections clearly show evidence of a tidal beam. It crosses the vertical line that depicts the position of station 6 at depths between 800 m and 1100 m. Both velocities reveal gradual change of the wave phase across the beam: u-velocity changes from negative to positive, and v-velocity changes its sign from positive to negative in the direction of wave phase propagation perpendicular to the beam (shown by the arrows C_p).

Position of the tidal beam predicted by the model is consistent with the available observational data. The velocity profiles u and v recorded at CTD station 6 (Figure 3 c) show the presence of local extremums in the water layer between 800 m and 1150 m (shaded yellow rectangle in the right panel) that can be associated with the beam. It is significant that the u and v extremums have opposite signs, exactly as the MITgcm predicts for the layer with the tidal beam. Note, however, that the observational velocity v does not remain negative above 800 m depth as the model predicts, but changes it sign to positive which could be evidence of a slope current which is not included in the model.

Further evidence of the beam generation was found in the velocity time series recorded at moorings La and Lb. The moorings were deployed closer to the shelf break (closer with respect to CTD station 6, Figure 2), specifically, in the area between points **a** and **b**, Figure 2 a, where the tidal beam is generated and is attached to the bottom. As a result, strong baroclinic tidal signal, produced by the beam, should be recorded in the bottom layer.

Figures 4 a and 4 c show 3.5-day time series of zonal and meridional velocities recorded at moorings La and Lb. The model predicted velocities for the same positions are presented in Figures 4 b and 4 d. As it was expected from the qualitative analysis, strong intensification of tidal currents is evident in the bottom 600-800 m layer at mooring La, both in experimental and model data (panels a and b). This intensification is accompanied by the change of the wave phase in the direction from the bottom upward, Figures 4 a and 4 b, which is a specific property of tidal beams.

Intensification of the velocity signals at the bottom are visible also in the model and experimental time series for the mooring Lb, although usage of two ADCPs (up-, and down-looking) with different sampling intervals (15 sec and 60 min, see Table 1) complicates the analysis and does not provide a smooth transition between two patterns (find white horizontal stripes at the depths 390-400 m in Figure 4 c) as it was for the mooring La. As a result, the theoretical and observational signals at the mooring Lb are less consistent.

Section 2.

Velocity time series recorded at mooring Sb and the model output for this location presented in Figure 5 a and 5 b do not reveal an overwhelming intensification of bottom currents associated with the tidal beam. Stronger bottom currents are still evident in v-component time series every second tidal cycle, Figure 5 a, but u-component is much weaker and does not show similar tendency. The model output reveals two fragments of strong bottom currents of v-velocity at t=0.8 day and 1.8 day, Figure 5 b, but u-velocity has all its maxima at the free surface over the whole period. This result does not completely support the conclusions of the qualitative analysis which suggests similar tidal signal for both mooring, Lb and Sb (see Figures 2 a, and 2 b).

In this respect it worth mentioning here that the qualitative analysis of the generation mechanism presented schematically in Figure 2 is based on a two-dimensional (2D) theory that ignores any three-dimensional (3D) effects. As it was shown above, a 2D approach works perfectly well for section 1 where the topography is slightly curved, but nearly two-dimensional. As distinct from the moorings La and Lb, the mooring Sb was deployed in a canyon,

Figure 1, where 3D effects play a fundamental role in formation of tidal wave fields. They can lead either to focussing, or defocussing of tidal energy. The latter probably was the case with the mooring Sb that does not reveal strong bottom intensification of tidal currents.

It is interesting that the model output also does not show strong bottom currents in the canyon. The reason for this effect can be analysed separately (normally canyons are traps for tidal energy, *Vlasenko et al.* (2016)), but the consistency of the model output with in-situ data (except the fact that the ADCP time series are more noisy due to high frequency processes that are not captured by the model) looks promising for the current study showing that the model captures all main features of tidal cycle correctly.

3D effects develop locally in canyons and attenuate in the far field and can not suppress completely the mechanism of tidal beam generation. As a confirmation of that, the velocity profiles recorded at CTD stations 37 and 45, conducted offshore of the canyon on 1400 m izobath, clearly show evidence of the tidal beam descending in the deep water, Figure 5 c and 5 d.

The tidal origin of these strong deep water currents can be confirmed by a simple comparison analysis. The time difference between velocity samples at stations 37 and 45 was 5 days 6 hours and 56 min (see Table 2). In terms of tidal activity it comprises 10.25 and 10.6 periods for two tidal harmonics, M_2 and S_2, respectively, or nearly 0.5 tidal cycle time lag on average. As one can see in Figures 5 c and 5 d, below 1000 m depth the velocity u is positive for station 37 and negative for station 45, and velocity v is negative for station 37 and positive for station 45, which should be valid for periodic processes when considering a half-period time lag.

Section 3.

Strong tidal beam signal at section 3 was not expected from the qualitative analysis, Figure 2. As a confirmation of that, the beam is not clearly observed in the model output and in the ADCP time series recorded at mooring Sd, Figure 6 a and 6 b. Overall, horizontal velocities observed at the mooring Sd are quite weak and polluted by a high frequency noise that is not present in the model signal. There are still two fragments with maximums of v velocity near the bottom in the middle of the theoretical time series, but general tendency is that the in-situ data and the model output reveal a dominantly barotropic tidal signal.

Apart from sharp edge topography discussed in previous section, another reason for a weak tidal energy conversion in section 3, could be the weak stratification in the layer of tidal beam generation. The inset into Figure 1 shows that the buoyancy frequency at the depths of 200-250 m (the place of the beam generation) has a local minimum.

Note, however, that in the abyssal part of section 3 the beam is quite visible. As evidence of that, the instant vertical profiles of horizontal velocities recorded at CTD station 14 (located seaward from Sd mooring, see Figures 1) do not reveal any notable activity in the layer between 400 m and 500 m depth, but demonstrate an overwhelming signal below 700 m with local maximums of both components at the depth of about 800 m, Figure 6 c. A realistic explanation of the absence of the tidal beam signal at mooring Sd and its presence in the deep part, could be an assumption that the tidal beam in this section is generated deeper than the 500 m isobath.

6. 3D deep water dynamics

The prior cross-section analysis has shown that although the 2D theory is a good tool for a qualitative analysis, it is not always applicable to realistic 3D problems. As demonstrated, the tidal characteristics in all three sections is quite different, and the main reason for that could be the substantial three-dimensionality of the bottom topography. It is postulates here that the bottom promontory depicted in Figure 7 by a green rectangular box, could be the reason for observed along-slope variability of the baroclinic tidal fields.

This variability is clearly seen in the deep water below 700 m depth. Figure 8 shows evolution of the temperature field in the vertical sections depicted in Figure 7 by red line. The temperature fields in this time series, Figure 8, were taken with 2-hour time interval. It show an internal wave structure that propagates in the north-east direction from the promontory. The crest of this wave is marked by an ellipse. An estimate of the wave phase speed based on Figure 8 gives the value 0.57 ms^{-1}.

Another estimates of the wave parameters can be done using Figure 9 which shows a plan view of a spatial distribution of the temperature for the northward propagating wave system at the depth of 1000 m. Temperature fields in this figure are given for the same time periods as in Figure 8. It is clear from Figure 9 that the wave system is attached to the slope. Its intensity decreases seaward revealing properties of a bottom trapped internal wave.

The wavelength can be estimated from the distance between the positions of the wave crest and the wave trough. The latter can be associated with the local minimum and maximum of the water temperature, respectively. Most clearly they are visible at the time moment 77 h. As it is shown in this panel, the distance $\lambda/2$ between the trough and crest is equal to 13.9 km. Assuming a semidiurnal tidal periodicity of the wave process one can estimate the phase speed as 0.64 ms^{-1}. Similar values calculated using just the positions of the trough and crest at different moment of time (the distance between the positions **a** and **b**, as well as **c** and **d**, see Figure 9) are 0.71 ms^{-1} and 0.61 ms^{-1}. Thus, all estimates give quite consistent values of the phase speed in the range between 0.57 ms^{-1} and 0.71 ms^{-1}. The average from all is equal to 0.62 ms^{-1}, which defines the wavelength as 26.8 km.

7. Analytical solution for bottom trapped internal waves

Numerical solution presented in Figures 8 and 9 are characteristic of a bottom trapped internal wave. The wave is confined to the bottom and exists only below 800 m depth; it propagates northward leaving the shelf to its right and its amplitude attenuates in seaward direction. To be confident that this interpretation is correct let's compare characteristics of the model predicted wave against analytical solution developed by *Huthnance* (1978). Here we restrict our discussion to the problem formulation and the final solution, assuming that more details can be found in the original paper.

A rotating basin of variable depth filled with stratified water at the latitude of 56° is considered. The horizontal axis $0x$ and $0y$ of the Cartesian coordinate system are taken seaward and along coastline, respectively. The vertical axis is oriented upward so that the water depth is defined as $z = -H(x)$, with uniform bottom topography in y direction. The coastline is set at $x = 0$. The bottom profiles $H(x)$ was taken by averaging of several zonal topography cross-sections in the area near the latitude of 56°, Figure

7 (sections a, b, c).

We are seeking for a periodic wave solution $\sim \exp[i(ky+\omega t)]$ with the wave-number k and frequency ω of the Boussinesq type equations for stratified incompressible fluid. For internal waves propagated along topography the governing system can be reduced to one equation for the pressure amplitude $P(x,z)$, i.e. the pressure $p(x,y,z,t) = P(x,z)\exp[i(ky+\omega t)]$:

$$\frac{\partial^2 P}{\partial x^2} + \frac{(1-\sigma^2)}{S}\frac{\partial}{\partial z}\left(\frac{1}{N^2}\frac{\partial P}{\partial z}\right) - l^2 P = 0, \tag{1}$$

with the following boundary conditions:

$$\begin{aligned}
\frac{dH}{dx}\left(\frac{\partial P}{\partial x} + \frac{l}{\sigma}P\right) + \frac{1-\sigma^2}{SN^2}\frac{\partial P}{\partial z} &= 0 \quad \text{at} \quad z = -H(x),\\
\frac{\partial P}{\partial z} &= 0 \quad \text{at} \quad z = 0,\\
P &\to 0, \quad \text{at} \quad x \to \infty,\\
kP - \sigma\frac{\partial P}{\partial x} &= 0 \quad \text{at} \quad x = 0.
\end{aligned} \tag{2}$$

Here $l = kL$ and $\sigma = \omega/f$, are a non-dimensional wave number, and non-dimensional frequency, respectively.

A wide variety of oceanographic situations are discussed in (*Huthnance*, 1978), but we focus here on just one particular case that fits the Malin Sea slope conditions. A non-dimensional parameter that shows relative contribution of rotation and stratification to the wave process is the Burger number, $S = (N_{\max}H/fL)^2$, where H_0 and L are the scales for the depth and slope width, respectively, $N_{\max}$ is the maximum of the buoyancy frequency, and f is the Coriolis parameter. Bearing in mind that the considered wave process develops below 800 m depth, the maximum of the buoyancy frequency can be taken $N_{\max} = 3 \cdot 10^{-3}\,\mathrm{s}^{-1}$ (see Figure 1). For two other parameters we can take: L =40000 m and H_0 =2000 m. Then the Burger number can be estimated as $S \cong$1.2.

An analytical solution for the bottom-trapped internal waves with the wave number k was obtained by *Huthnance* (1978) for the conditions when $1/(kL) < S^{-1/2} < 1$. As it was found in the previous section, the wavelength of the model predicted wave can be estimated as 26.8 km, i.e. parameter $1/(kL) \cong$0.11. For the Burger number S =1.2 the value $S^{-1/2}$=0.91, i.e. theory by *Huthnance* (1978) can be applied to the Malin Seas slope area.

For relatively short-scale topographically trapped internal waves with the wavelength in the range between 10 km and 30 km, the solution of (1)-(2) reads:

$$P(x,z) = H_m(\beta(x)) \exp\left[-\frac{\beta^2(x)}{2}\right] \exp\left[-k\frac{z+H(x)}{\sqrt{\phi(z)+\left(\frac{dH}{dx}\right)^2}}\right], \quad (3)$$

where H_m is the Hermite function of the $m-$th order,

$$\beta(x) = (x-x_0)\frac{N\mathrm{max}H_0}{f}\left[\frac{\left(\frac{dH}{dx}\right)^2\frac{d^2\phi}{dz^2}}{2\phi(z)} - \frac{\frac{d^3H}{dx^3}}{\frac{dH}{dx}}\right]_{(x_0,z_0)},$$

$$\phi(z) = \frac{(f^2-\omega^2)}{N^2(z)}\left(\frac{L}{H_0}\right)^2.$$

Here (x_0, z_0) are the coordinates of the sea bed point where the product $N(z)\frac{dH(x)}{dx}$ has maximum value. For the bottom profile under consideration here the maximum of buoyancy frequency (or main pycnocline) is the depth where the core of the bottom trapped wave should be expected.

Figure 10 presents first three normalized amplitude functions $P(x, z)$ of solution (3). The calculations were done for the frequency ω that corresponds to M_2 tide and the wavelength 26.8 km. For node $m = 0$ the solution has one maximum located at the bottom with its centre at the isobath of 1200 m. Centres of node $m = 1$ and mode $m = 2$ solutions are located nearly at the same depth, but they have two and three maximums, respectively.

In order to understand which of the nodes was generated in the numerical model over the Malin Sea slope one can analyse the position of amplitude of the propagated wave. In doing so, the field of the amplitude velocities

$$a = \sum_{j=1}^{12} \sqrt{u^2(j) + v^2(j)}/12;$$

along three vertical sections shown in Figure 7 has been calculated. Here $u(j)$ and $v(j)$ are zonal and meridional model predicted amplitude velocities taken over one tidal period.

Figure 11 shows the a field for three vertical sections presented in Figure 7 by blue dotted lines. Apart from a totally expected intensification of barotropic tidal currents in the shallow water area to the right of the longitude 9.4°W, two localised spots of intense baroclinic tidal motions can be identified in Figure 11 c. One of these areas can be classified as a tidal beam traced in this panel by a characteristic line of the wave equation depicted by solid black line. The red spot attached to the bottom between 9.45°W and 9.65°W (marked by a magenta ellipse) has nothing to do with the tidal beam. It exists separately attached to the bottom where trapped internal wave propagates.

In the middle section (Figure 11 b) these two objects still exist separately below 800 m, but above this depth they merge. In the northernmost section a (Figure 7) the bottom trapped wave is less intense (see Figure 11 a), but it is still visible as bottom intensified current. Assuming that Figure 11 shows evidence of the bottom trapped internal wave, one can conclude from its compact structure that it represents node $m = 0$ of solution (3) of the boundary value problem (1)-(2). Comparing Figures 11 with upper panel of Figure 10 one can find quite a good consistency, both in spatial structure, and in the depth of its location, specifically in the area where $N(z)H'(x)$ takes the maximum value.

8. Discussion and conclusions

The properties of bottom trapped waves can be treated in terms of theory developed by *Wang and Mooers* (1976). According to their classification internal waves in stratified water can exist with scales of internal Rossby radius that propagate in a basin of nearly constant depth. On the other hand, in homogeneous ocean with an inclined bottom the topographic shelf waves can exist. In real ocean water stratification and inclined bottom exist together. This can lead to the generation of a hybrid type waves, so called bottom trapped waves, that have properties of both. The frequency of Rossby wave is always below the inertial frequency $f = 2\Omega \cos\phi$ ($\Omega = 0.0000729\,\mathrm{s}^{-1}$ is angular velocity of Earth rotation and ϕ is the latitude). However, the zero mode internal Kelvin wave can exist both below and above critical latitude, having M_2 tidal period, in particular.

The most typical mechanism for generation of bottom trapped internal waves is scattering of internal wave propagating along corrugated topography.

Interacting with a prominence a superinertial internal wave ($\omega > f$) transforms its energy to a system of scattered internal waves freely radiated in all directions from the topography feature (see *Chapman* (1982), for instance). However, as it was shown by *Huthnance* (1978); *Dale and Sherwin* (1996); *Dale et al.* (2001), if the wave frequency is close to the inertial one (as in our case, $\sigma/f = 1.178$), the wave is "nearly" trapped by the topography. In other words, the energy of the incident wave is split into two parts, one goes to internal Poincare modes radiated from the source of generation, and another one to the topography trapped internal wave propagating along the coast leaving the coastline to its right (in the northern hemisphere). Moving closer to the inertial frequency, less energy is transformed to the radiated Poincare modes. The vertical structure of these waves depends both on slope/shelf topography and fluid stratification.

All these theoretical issues are highly relevant for explanation of bottom intensification of tidally induced baroclinic currents observed in the 88-th cruise of the RRS "James Cook" over the Malin Sea continental slope and reproduced numerically using the MITgcm. The reported data has quite a realistic explanation in terms of superposition of two energetic processes developing in the area. One of them is a bottom trapped internal wave generated by the tidal flow at a local bottom prominence and propagated along the slope (Figures 7-9). The maximum currents associated with this type of motions were located near the bottom at the depths below 800 m. The intensity of the currents decreased from its centre both upward and horizontally from the core. The analysis of the position of the bottom current and its spatial distribution allows one to conclude that recorded in-situ and predicted numerically baroclinic processes with good accuracy can be treated in terms of analytical solution (3) presenting a zero-node bottom trapped internal wave (its spatial structure is shown in Figure 10 a).

The second class of motions identified over the Malin Slope is a baroclinic tidal beam that is usual feature of internal tidal fields in the area of steep (supercritical) topographies. The beam is normally generated at the shelf break and radiates tidal energy into abyss along the characteristic lines of the internal wave equation. Evidence was found for this in both the observational data set and in the model output (Figure 11, for instance).

It is worth noting that the properties of the tidal beam were discussed here only for the three cross-slope sections where the observational data were available. However, assuming the more complicated three-dimensional dynamics, one can learn more from the model output on the spatial characteristics of the tidal beam. Figure 12 shows that the tidal beam can be detected in much wider area than that occupied by the bottom trapped internal wave. The tidal beam is not visible in the temperature fields in Figure 9 which allowed identification of the bottom trapped wave. However, the more energetic horizontal motions presented in Figure 12 illustrate the seaward propagation of the tidal beam phase over the whole area during one tidal cycle quite clearly. The along slope stretched blue area of negative eastward velocity u visible at t=73 h migrates seaward over next 6 h being gradually replaced near the slope by the red colour (positive velocity) stripe that also moves seaward. A distinguishing feature of the tidal beam, i.e. downward radiation of baroclinic tidal energy, can also be identified in Figure 12. The left-top corner of each panel in this figure do not reveal strong variation of horizontal velocity suggesting that the tidal beam in this area is located much deeper.

There is also a possibility to record the waves arrived to the Malin Shelf from some distant sources of generation, the Rockall Bank or the Anton Dohrn Seamount, for instance. Such events were observed from space (*Small et al.*, 1999b) and analysed theoretically (*Stashchuk and Vlasenko*, 2005). Note, however, that in light of the present study which focuses on the bottom trapped internal waves, such a scenario is considered as less probable than local generation, although some further work would be necessary to address this issue.

Overall, it is not always easy to separate with certainty the along slope propagated bottom trapped waves from downward radiated tidal beams. An obvious criteria for such spatial separation would be the fact that bottom trapped internal waves always have their maximum velocities at the bottom, Figure 10, whereas the beams always detach from the place of generation having maximums of their velocities in the intermediate layers, Figure 11. However, in the areas where the beam is generated (shallower 1000 m isobath) these two processes develop together and contribute equally to the bottom current intensification. As an illustration of that, Figure 13 shows a spatial distribution of the amplitude of horizontal velocity in the bottom layer. Only joint analysis with Figure 11 allows us to conclude that the bottom trapped internal waves are responsible for intensification of bottom currents deeper 1000 m isobath (find red spot in the top right corner of Figure 13) but shallower this depth mostly the tidal beam contributes to bottom currents.

Analysis conducted here illustrates evidence of three-dimensional baroclinic wave dynamics (such as bottom trapped internal waves and 3D tidal beams) developing over the Malin Sea continental slope. Importantly, considered here configuration of bottom topography is not unique to this study and is expected to have global significance.

Acknowledgments This work was supported by the Natural Environment Research Council grant FASTNEt (award NE/I030259/1). We thank Dr. Justin Small, Dr. Mark Davidson and two anonymous reviewers for their valuable advises.

References

Chapman, D.C. (1982) Nearly trapped internal edge waves in a geophysical ocean. *Deep Sea Res.*, *29*, 525-533.

Dale, A.C., and T.J. Sherwin (1996) The extension of baroclinic coastal-trapped wave theory to superinertial frequencies, *J. Phys. Oceanogr.*, *26*, 2305-2315.

Dale, A.C., J.M. Huthnance, and T.J. Sherwin (2001) Coastal-trapped internal waves and tides at near-inertial frequencies, *J. Phys. Oceanogr.*, *31*, 2958-2970.

Egbert, G.D., and S.Y. Erofeeva (2002) Efficient inverse modeling of barotropic ocean tides, *J. Atmos. Oceanic Technol., 19(2)*, 183–204.

Falahat,S., and J. Nycander (2015) On the generation of the bottom trapped internal tides. *J. Phys. Oceanogr.*, *45*, 526-545.

Hallock, Z.R., J. Small, J. George, R.L. Field, and J.C. Scott (2000). Shoreward propagation of internal waves at the Malin Shelf edge, *Cont. Shelf Res.*, *20*, 2045-2057.

Huthnance, J.M. (1978) On coastal trapped waves. Analysis and numerical calculations by inverse iterations, *J. Phys. Oceanogr.*, *8(1)*, 74-92.

Inall, M.E., T.R. Rippeth, and T.J. Sherwin (2001). Impact of nonlinear waves on the dissipation of internal energy at the shelf break, *J. Geophys. Res.*, *105*, 8687-8705.

Inall, M.E., T.R. Rippeth, and T.J. Sherwin (2001). Observations of the internal tide and associated mixing across the Malin Shelf, *J. Geophys. Res.*, *107*, C4, 3028, 10.1029./2000JC000761.

Inall, M.E., G.I. Shapiro, and T.J. Sherwin (2001). Mass transport by non-linear internal waves on the Malin Shelf, *Cont. Shelf Res.*, *21*, 1449-1472.

Lerczak, J.A., C.D. Winant, and M.C. Hendershott (2003) Observations of the semidiurnal internal tide on the California slope and shelf, *J. Geophys. Res.*, *108*, doi:10.1029/2001JC001128.

Marshall, J., A. Adcroft, C. Hill, L. Perelman, and C. Heisey (1997) A finite-volume, incompressible Navier-Stokes model for studies of the ocean on the parallel computers, *J. Geophys. Res.*, 102, 5733-5752.

Pacanowski, R.C., and S.G.H. Philander (1981) Parameterisation of vertical mixing in numerical models of Tropical Oceans. *J. Phys. Oceanogr.*, *11*, 1443-1451.

Rhines, P.B. (1970) Edge, bottom,, and Rossby waves. *Geophys. Fluid Dyn.*, *1*, 273-302.

Sherwin, T.J., and N.K. Taylor (1990). Numerical investigations of linear internal tide generation in the Rockall Trough, *Deep Sea Res.*, *37*, 1595-1618.

Sherwin, T.J. (1988) Analysis of internal tide observed on the Malin Shelf, North of Ireland, *J. Phys. Oceanogr.*, *18*, 1035-1050.

Small, J., T.Sawyer, and J. Scott (1999). The evolution of an internal bore at the Malin shelf break, *Annales Geophysicae*, *17*, 547-563.

Small, J., Z. Hallock, G. Pavey, and J. Scott (1999). Observations of large amplitude internal waves at the Malin Shelf edge during SESAME 1995, *Cont. Shelf Res.*, *19*, 1389-1436.

Small, J. (2000). The refraction, shoaling and structure of non-linear internal waves at a continental shelf margin. *PhD Thesis from National Oceanography Centre (formerly Southampton Oceanography Centre)*. Available at http://eprints.soton.ac.uk/42171/1.hasCoversheetVersion/0000393.pdf

Small, J. (2004). The refraction and shoaling of non-linear internal waves at the Malin Shelf break, *J. Phys. Oceanogr.*, *33*, 2657-2674.

Souza, A.J., J.H. Simpson, M. Harikrishnan and J. Malarkey (2001), Flow structure and seasonality in the Hebridean slope current, *Oceanologica Acta*, *24*, 63-76.

Stashchuk, N., and V. Vlasenko (2005). Topographic generation of internal waves by nonlinear superposition of tidal harmonics, *Deep Sea Res.*, *52*, 605-620.

van Haren, H. (2009) Using high sampling-rate ADCP for observing vigorous processes above sloping [deep] ocean bottoms. *J. Mar. Sys., 77*, 418-427.

Vlasenko V., N. Stashchuk, and K. Hutter (2005), Baroclinic tides: theoretical modeling and observational evidence. Cambridge University Press. 365 pp.

Vlasenko V., N. Stashchuk, M.Inall, and J.Hopkins (2014), Tidal energy conversion in a global hot spot: on the 3D dynamics of baroclinic tides at the Celtic Sea shelf break, *J. Geophys. Res.*, *119(6)*, 3249–3265, doi:10.1002/2013JC009708.

Vlasenko V., N. Stashchuk, M.Inall, and D.Aleynik (2016), Focusing of baroclinic tidal energy in a canyon *J. Geophys. Res.*, *121(4)*, 2824–2840.

Wang, D.-P., and C.N.K. Mooers (1976) Coastal-trapped waves in a continuously stratified ocean. *J. Phys. Oceanogr.*, *6*, 853-863.

Xing, J., and A. M. Davies (1997). The influence of wind effects upon internal tides in shelf edge regions, *J. Phys. Oceanogr.*, *27*, 21002125.

Xing, J., and A. M. Davies (1998). Formulation of a three-dimensional shelf-edge model and its application to internal tide generation, *Cont. Shelf Res.*, *18*, 405-440.

Xing, J., F. Chen, and R. Proctor (1999). A two-dimensional slice model of the shelf edge region off the west coast of Scotland: model response to realistic seasonal forcing and the role of the M2 tide, *Cont. Shelf Res.*, *19*, 1353-1386.

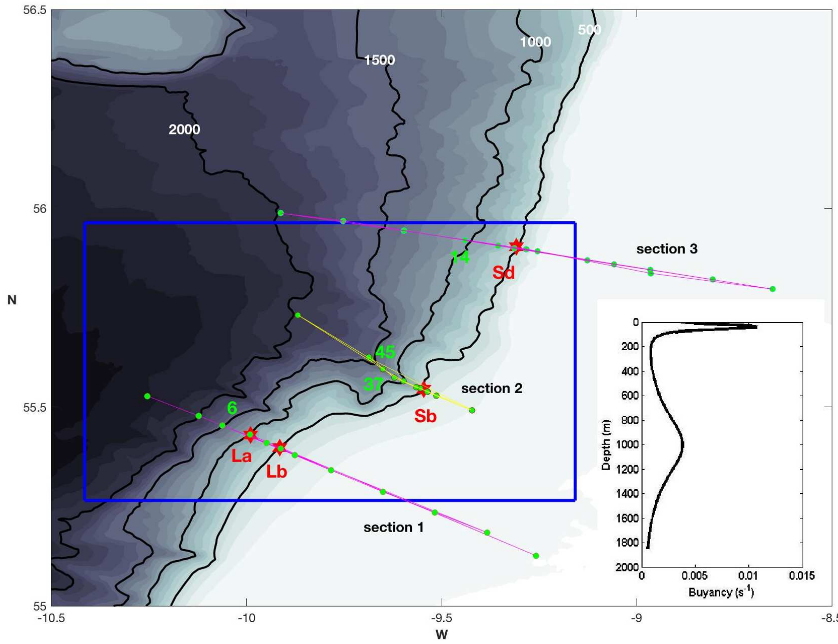

Figure 1: Bathymetry of the Malin Sea with the plan view of the JC88 field experiment. Green closed circles show positions of the CTD stations; red hexagrams depict the positions of moorings. Blue rectangle shows the model domain. Buoyancy frequency averaged over CTD stations is shown in the inset.

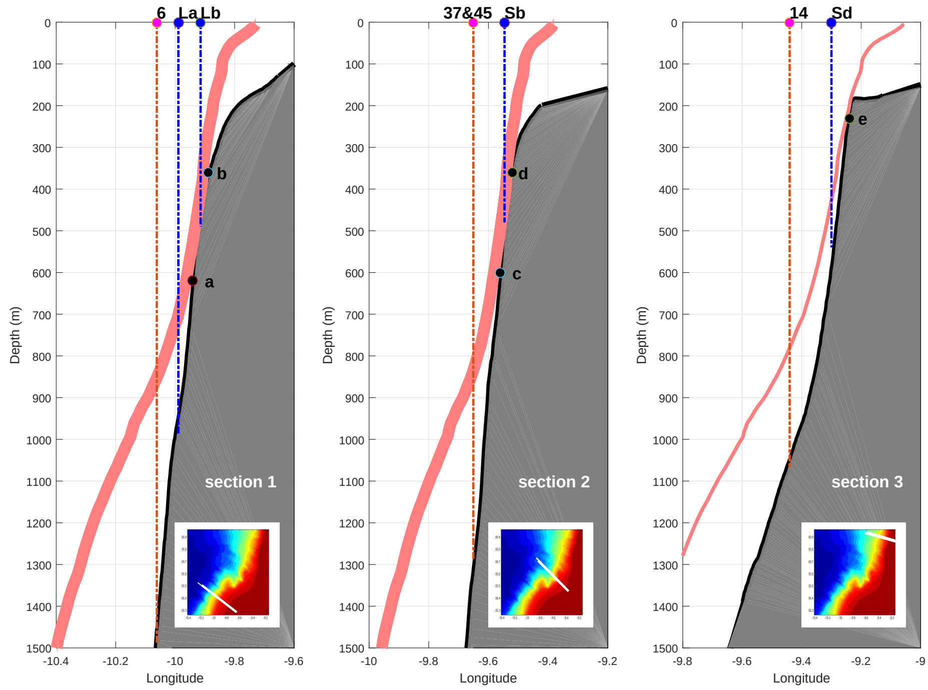

Figure 2: Bottom topography along sections 1, 2, and 3 (from the left to the right) depicted in Figure 1. Location of moorings Lb, Sb, Sd, and CTD stations 6, 37, 45, & 14 are shown by vertical dash-dotted lines. Red lines show positions of a tidal beam.

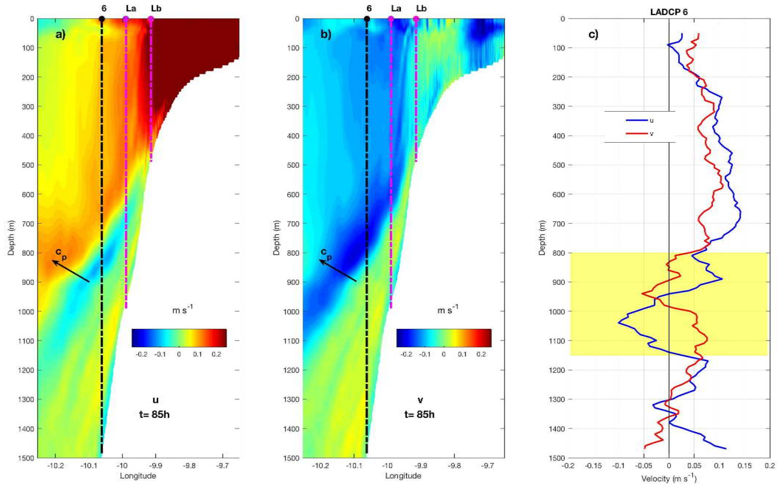

Figure 3: Section 1 (see Figure 1): Model predicted zonal u (a) and meridional v (b) horizontal velocities for the time moment t =85 h of the model run. The characteristic line is shown by the black dotted line. (c) Instant vertical profiles of u and v velocities recorded by LADCP at CTD station 6.

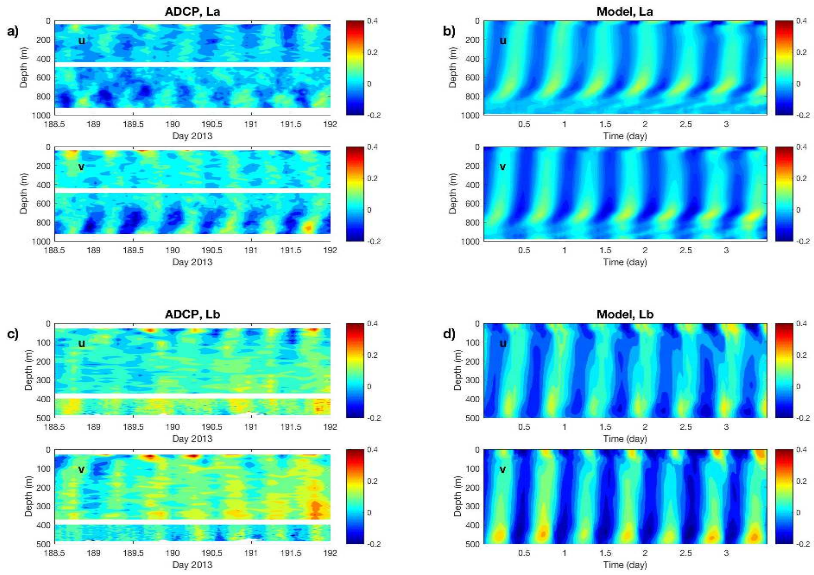

Figure 4: Zonal u and meridional v velocity time series recorded at moorings La (panel a) and Lb moorings (panels c). Corresponding model predicted time series are shown in panel (b) and (d), respectively.

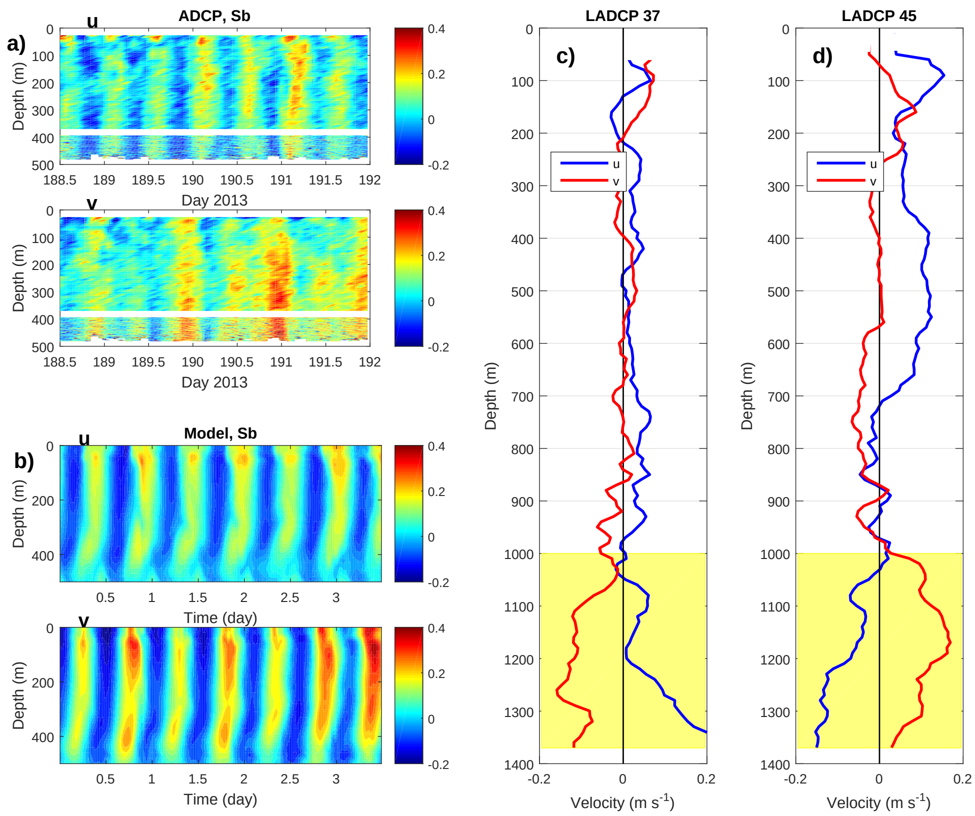

Figure 5: Zonal u and meridional v velocity time series recorded at Sb mooring by a) ADCP and b) the model. c) Instant u and v velocity profiles measured at stations 37 and 45.

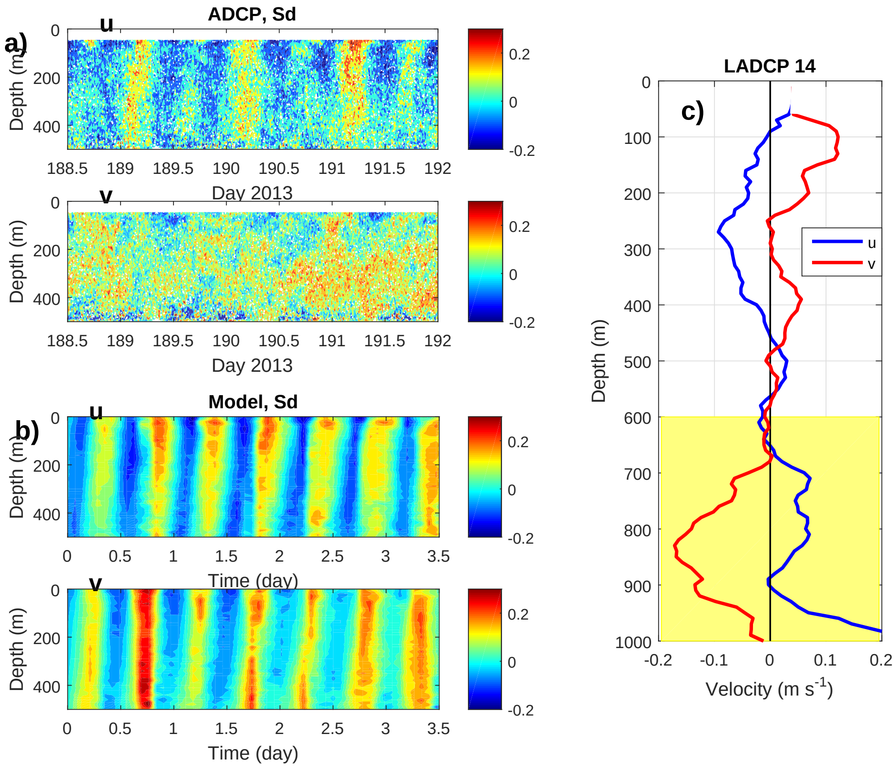

Figure 6: Zonal u and meridional v velocity time series recorded at Sd mooring by a) ADCP and b) the model. c) Instant u and v velocity profiles measured at CTD station 14.

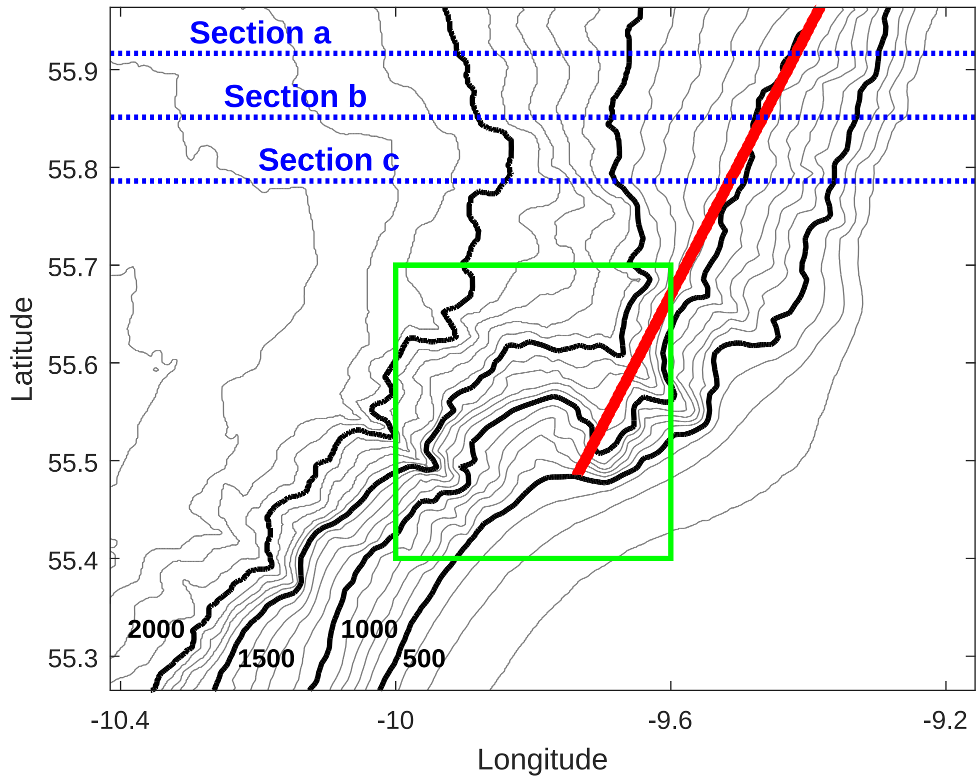

Figure 7: Bottom topography with sections used in the analysis.

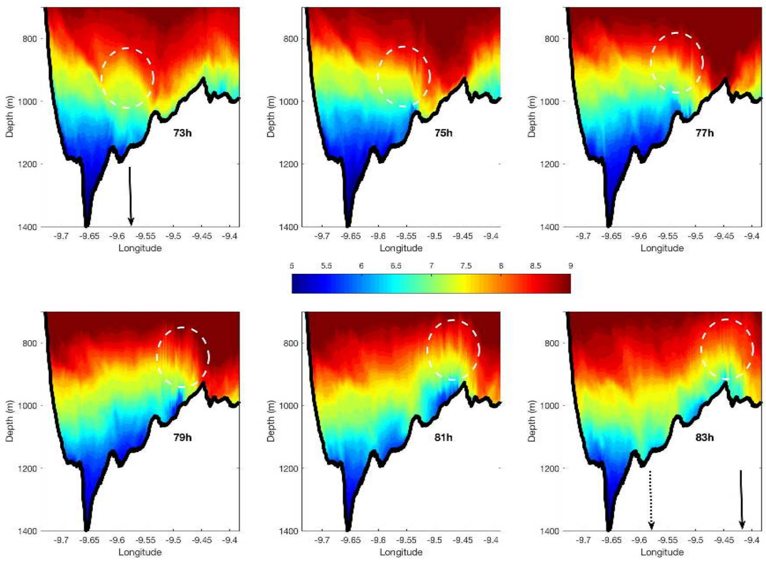

Figure 8: Model predicted evolution of the temperature field along the vertical section shown in Figure 7 by red line. The time span covers interval from t =73 h to t =83 h of the model time. White dashed ellipses depict the positions of the wave crest.

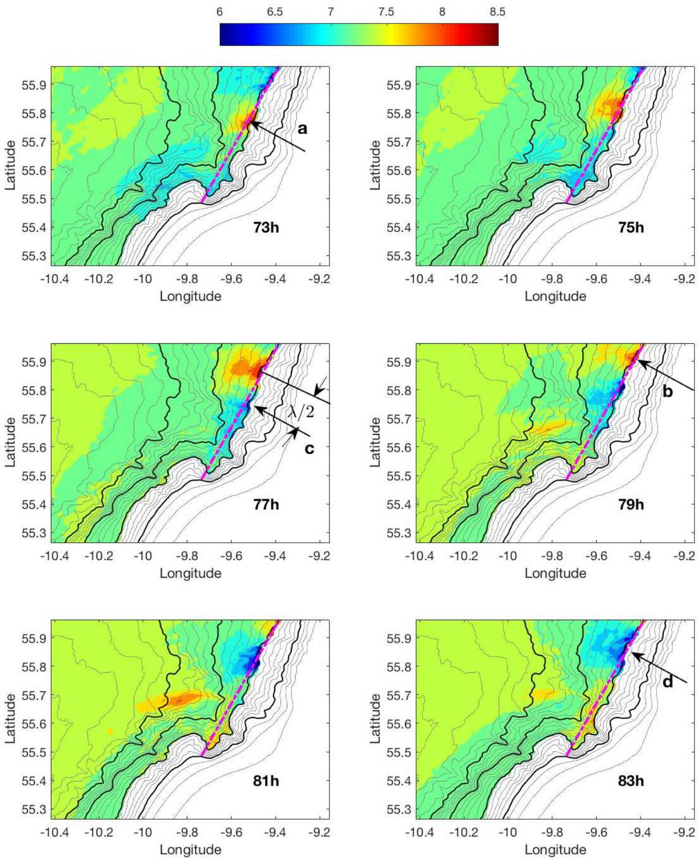

Figure 9: Model predicted temperature at 1000 m depth. Model time is shown in right bottom corner of each panel. Black arrows show positions of troughs (red spots) and crests (blue colour) of the bottom trapped internal wave.

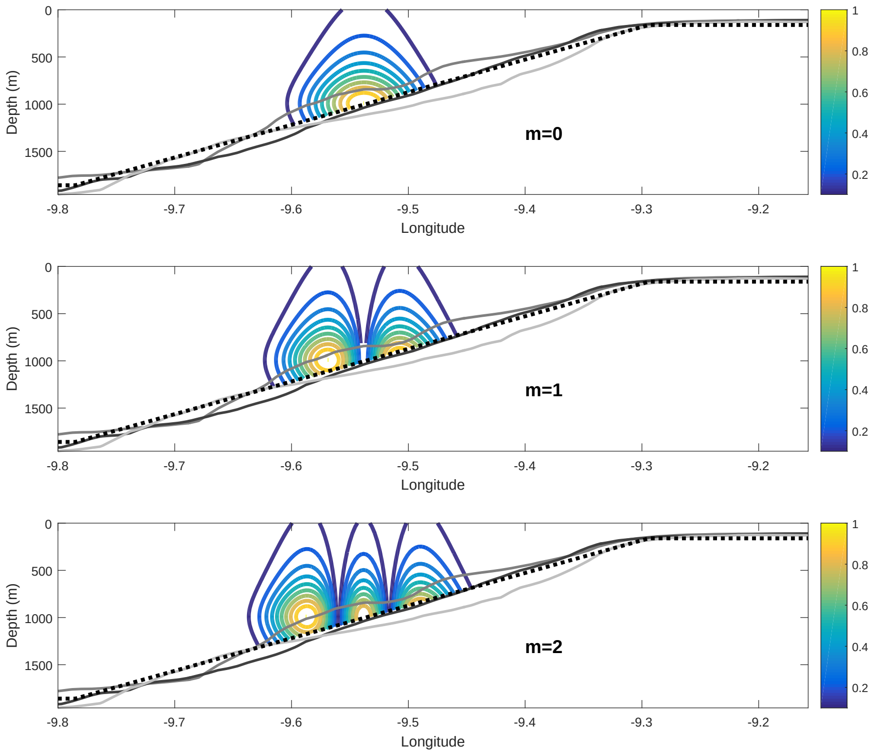

Figure 10: Three first normalized eigen functions $P(x,z)$ of the boundary value problem (1)-(2). Dotted line shows the bottom topography calculated as an average from several profiles presented in the figure.

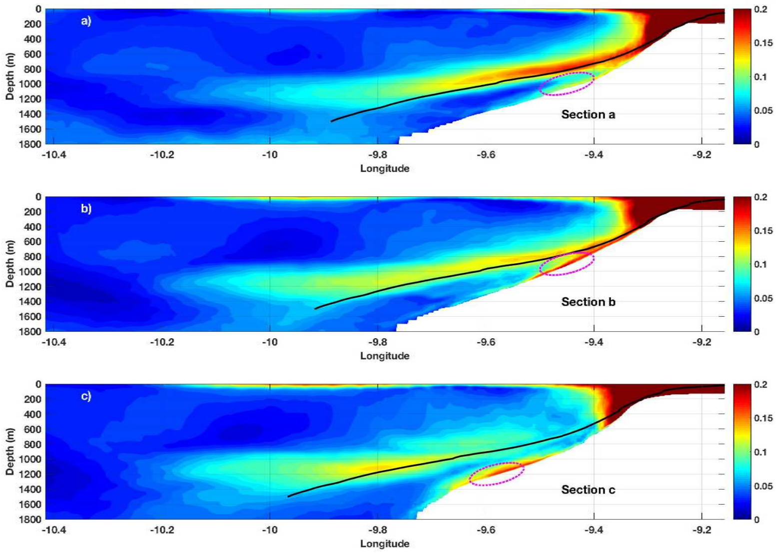

Figure 11: Model predicted amplitude of horizontal velocities for zonal sections a) 55.9166°, b) 55.8513° and c) 55.786° shown in Figure 7. Positions of the bottom trapped internal wave are shown by the magenta ellipses. The direction of the tidal beam is depicted by the black lines.

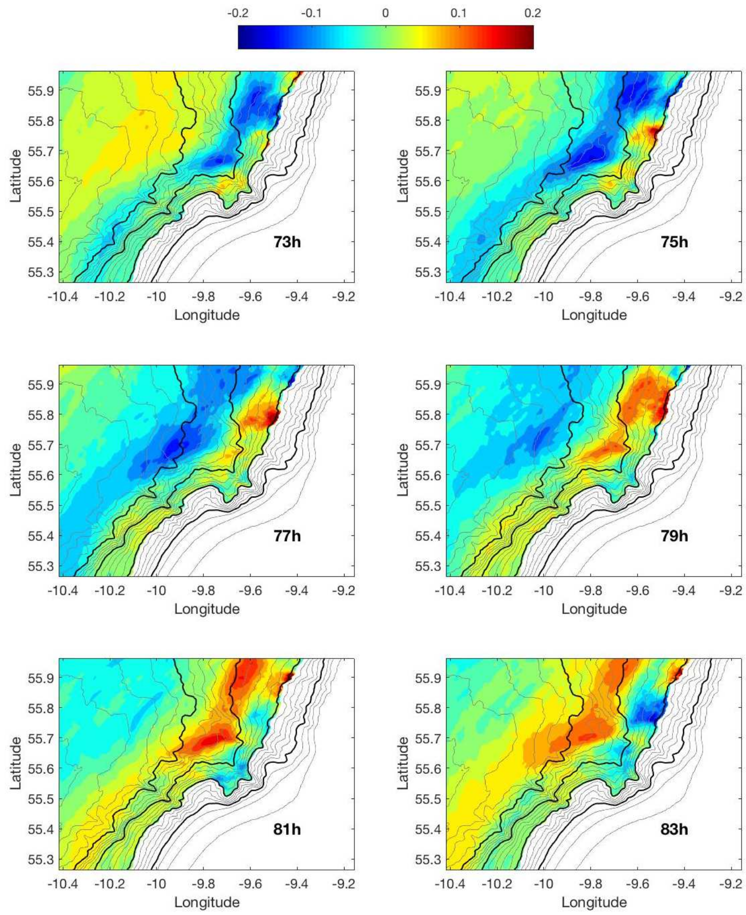

Figure 12: Model predicted u-velocity at 1000 m depth. Time span is shown in right bottom corner of each panel.

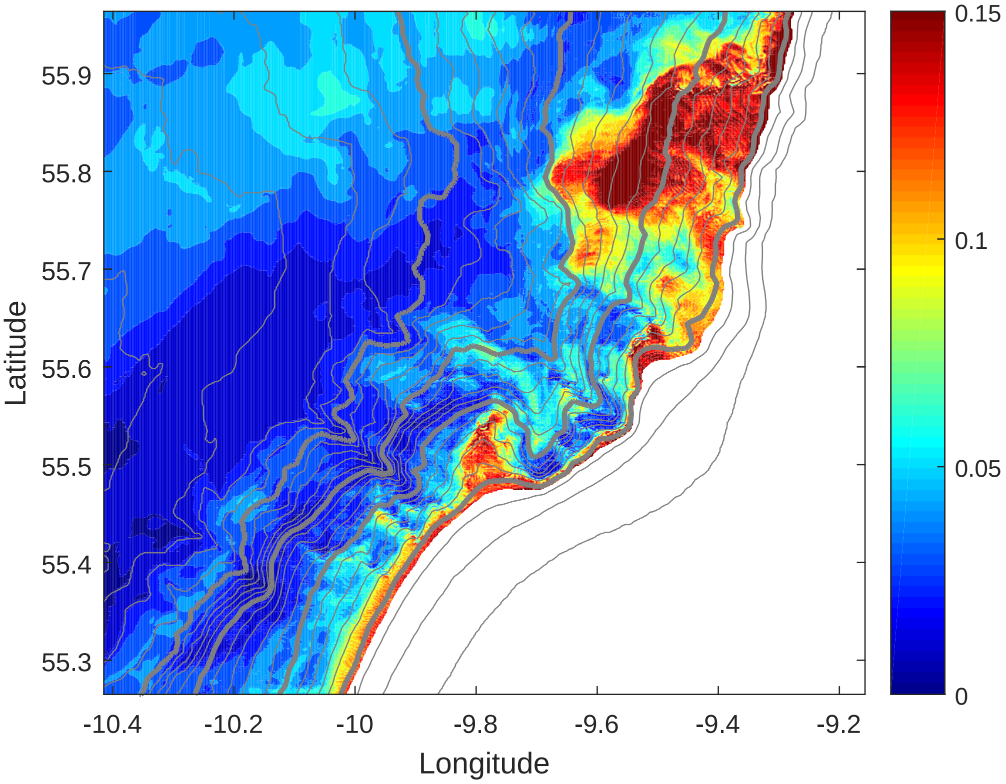

Figure 13: Model predicted amplitude of horizontal velocity (ms^{-1}) 10 m above the bottom overlaid with bottom topography.

Table 1: CTD stations details

Name	Latitude	Longitude	Date	Time	Depth (m)
06	55°27.23′	010°03.69′	01/07/2013	07:00	1483
37	55°35.761′	009°39.037′	06/07/2013	22:36	1380
45	55°35.760′	009°39.041′	12/07/2013	05:31	1384
14	55°55.229′	009°26.42′	02/07/2013	22:32	1044

Table 2: ADCP mooring data

Name	Instrument	Up/Down	Depth (m)	Sample interval
La	ADCP 75KHz	U	467.5	60 min
	ADCP 75KHz	D	472	60 min
Lb	ADCP 75KHz	U	391	60 min
	ADCP 300KHz	D	394.5	15 sec
Sb	ADCP 75KHz	U	387.5	5 min
	ADCP 300KHz	D	389	15 sec
Sd	ADCP 75KHz	U	544	2.5 min

Table 3: Tidal data

	M2	S2	N2	K2	K1	O1	P1	Q1
$A(\mathrm{m}^2\mathrm{s}^{-1})$	30	14	8.2	3.5	1.78	0.98	0.67	0.56
ϑ(degr)	143	127	75	102	170	0	39	18
$B(\mathrm{m}^2\mathrm{s}^{-1})$	25	9.14	7.18	2.79	3.11	1.32	1.09	0.9
θ(degr)	28	180	125	146	115	63	78.5	47.5